Desiccation Crack Formation Beneath the Surface

B. Zhao, J.C. Santamarina

King Abdullah University of Science and Technology (KAUST), Thuwal, Saudi Arabia.

Abstract. Desiccation cracks affect all mechanical and conduction properties. Previous studies have investigated the formation of surface desiccation cracks in fine-grained sediments in relation to their compressibility and suction potential. This study explores the formation of internal desiccation cracks in saturated kaolinite specimens consolidated inside self-reactive oedometer cells to reproduce the initial effective stress in buried sediments. We use X-ray tomography to monitor internal processes during consolidation and drying. Images capture the evolution of a perimetric fracture, transverse contraction, volumetric changes in entrained gas bubbles, and the development of internal desiccation cracks. Entrained gas bubbles act as nucleation sites. They shrink during loading and early stages of desiccation. Eventually, the gas-water interface penetrates the soil at the bubble surface, pushes particles away, enlarges local pores and facilitates further growth of the internal desiccation crack. While air entry is grain-displacive in soft fine-grained sediments, it becomes pore-invasive in stiff coarse-grained sediments and internal desiccation cracks are not expected in silts or sands.

Keywords: Clays, Compaction, Laboratory tests, Partial saturation, Suction

Submit to: Géotechnique (Technical Note)

Corresponding Author: Budi Zhao (budi.zhao@kaust.edu.sa)

1. Introduction

Fine-grained sediments are susceptible to desiccation crack formation because of their high compressibility and suction potential. Desiccation cracks nucleate at large surface pores where air invades the water-saturated sediment (Scherer, 1990; Shin & Santamarina, 2011a; Cordero et al., 2017). Restrained lateral shrinkage hinders horizontal contraction, facilitates air invasion and leads to the extensive fracture patterns observed in drying thin mud layers.

Can desiccation cracks nucleate and grow within the sediment, beneath the surface? Subsurface syneresis cracks can develop due to changes in pore fluid salinity (Plummer & Gostin, 1981) or earthquake-induced dewatering (Pratt, 1998). Internal cracks have been reported in laboratory desiccation tests where cracks nucleated at the centre or at the bottom boundary of specimens (Corte & Higashi, 1960; Lakshmikantha et al., 2018). Internal fracture formation would be relevant to many engineering applications, such as nuclear buffers, compacted liners (Yesiller et al., 2000), embankment dams (Sherard, 1986; Dyer et al., 2009), seal layers for CO_2 storage (Espinoza & Santamarina, 2012), and giant desiccation cracks (Harris, 2004). This study focuses on desiccation cracks that nucleate around internal gas bubbles. Possible formation mechanisms for gas bubbles include entrapment during sedimentation, bioactivity, anaerobic oxidation, and gas exsolution during suction-driven depressurization.

There are no published studies on the evolution of internal gas bubbles during desiccation and their role in internal crack nucleation. This experimental study investigates the desiccation of kaolinite specimens under confinement to reproduce various burial depths. We keep entrapped air bubbles as potential nucleation sites and use X-ray tomography to see inside the confining vessel and monitor internal processes during drying.

2. Experimental Study

2.1. Materials

The kaolinite used in this study has liquid limits LL_{water}= 48%, LL_{brine}= 55%, and LL_{ker}= 74%, and is classified as a fine sediment of low plasticity and intermediate electrical sensitivity LP/IS in the Revised Soil Classification System (Jang & Santamarina, 2015; CL in USCS). We use a dewpoint hygrometer to determine the soil water retention curve (WP4C PotentialMeter; Campbell et al., 2007). The test starts with a paste prepared at $w\approx$ 1.2 LL; it dries at room temperature and homogenizes overnight between each recording of suction ψ and water content w. The specimen contracts during desiccation, therefore, the measured soil water characteristic curve reflects the evolving pore size distribution (Khalili et al., 2008). Air entry takes place at a suction $\psi_{AE}\approx$ 2.0 MPa (Fig. 1).

2.2. X-ray Tomographer

The custom-built X-ray tomographer can scan large and heavy specimens (max weight~ 300 N). The system consists of (1) a high power cone-beam source to see through specimens within vessels (Comet, MXR-225HP, 225 kV), (2) a high-resolution flat panel detector (Varian, PaxScan 1313Dx, size= 130×130 mm, 1024×1024 pixels), and (3) a precision rotation base for heavy specimens (Parker SM162BE-N10M motor and Parker R200M rotary stage; microstep δ= 0.005º). Pixel resolution ranges from 40 μm for 40 mm specimens, to 100 μm for 100 mm specimens.

2.3. Self-reacting Oedometer Cells

Three identical oedometer cells are made of aluminum to minimize X-ray attenuation (Fig. 2 – OD= 75 mm, H_0~ 100 mm, wall thickness t= 5 mm). Perforated plates and porous stones allow

65 water evaporation from both the upper and lower ends. The cell body includes a pneumatic cylinder
66 to apply the vertical load during specimen compaction and drying, and an LVDT to measure the
67 vertical displacement of the sediment. This self-reacting cell design allows moving the oedometer
68 between the environmental chamber and the tomographer without perturbing on-going processes.
69 The air pressure hose disconnects from the cell at the isolation valve for scanning (Fig. 2). The air
70 pressure remains almost constant in the pneumatic cylinder, and specimens are stable during
71 tomographic scans.

72 *2.4. Test Sequence*

73 Small air bubbles remain entrapped in the otherwise water-saturated kaolinite pastes
74 (mixed at w= 50%). We fill three chambers and consolidate specimens to different vertical stress
75 levels to reproduce various burial depths: σ'_{z0}= 10 kPa, 20 kPa, and 50 kPa. Then, let specimens
76 dry at room temperature (T= 25°C) for ~40 days. The second drying phase takes place in an
77 environmental chamber at T= 60°C (Fig. 3). We measure the specimen weights throughout the
78 drying process, and collect X-ray tomographic images at specific drying states.

79 *2.5. Image Processing*

80 The analysis of tomographic images involves three steps. First, we distinguish soil voxels
81 from air, aluminum, and porous stones with threshold values that maximize the variance of voxel
82 intensities between classes (Otsu method, Liao et al., 2001). We identify and label air bubbles to
83 track their development. Finally, we measure the volume of the soil matrix and individual air
84 bubbles. Calibration tests show that specimen volumes measured from X-ray tomograms deviate
85 by less than 1% from physically measured volumes, however the error on single small bubbles can
86 be higher than 1%.

3. Experimental Results

3.1. Vertical Strain and Water Content

Figure 3 shows the evolution of water content and vertical strain measured for the three specimens during the three experimental stages. Experimental results show:

- Loading stage: higher vertical strains and lower final water contents correlate with higher effective stress, in agreement with the consolidation response of this kaolinite.
- Drying at room temperature (~40 days, 38±2% < w < 50%): there is a limited decrease in water content and a minor vertical strain in all specimens. Suction remains low during this phase (ψ < 100 kPa, inferred from water contents and the soil water retention curve in Fig. 1).
- Drying in the environmental chamber at 60 °C (additional 40 days): the response becomes suction-controlled and the three specimens experience a similar vertical strain of approximately 5.2%. The water content decreases below the water content at air entry ($w_{\mathrm{AE}} \approx$ 24%). Finally, the vertical strains stabilize while the soil specimens finish drying.

3.2. Tomograms

We obtain high-resolution tomograms (95 μm voxel size) throughout the loading-desiccation history. Points shown on the vertical strain curves in Fig. 3 identify scanning events. Figure 4 presents two cross sections at different depths obtained at three different stages of drying. These images capture the evolution of the perimetric fracture and transverse contraction, changes in bubble geometry (slices across the equatorial plane of large bubbles), and the development of internal desiccation cracks. Internal cracks nucleate at gas bubbles (see arrows) at a water content similar to or lower than the water content at the air entry value AEV ($w_{\mathrm{AE}} \approx$ 24%, Fig. 1); a slice-by-slice examination confirms that these internal cracks are isolated and do not reach the external

soil boundaries. Bubbles near the perimeter are weak zones and alter the path of the perimetric fracture. Detailed analyses based on tomographic images follow.

3.3. Sediment Volume

Vertical strains are not sufficient to quantify the sediment volume contraction when desiccation cracks form. Therefore, we use the X-ray tomograms to track the sediment volume response. Fig. 5 plots the void ratio computed with the sediment volume from image analysis, against the Bishop stress computed for χ= 1.0, where suction values are estimated from the measured water contents and the soil water retention curve (Fig. 1). The void ratio vs. Bishop stress trend tracks the 1D consolidation response of water saturated kaolinite ($e_{1\mathrm{kPa}}$= 1.38, C_c= 0.18). Suction prevails over the initial vertical stress σ'_{z0} throughout the desiccation phase (Fig. 5). The consolidation trend breaks at the AEV, and a further increase in suction has a diminishing effect on the void ratio, i.e., Bishop's effective stress parameter $\chi \rightarrow 0$. These results suggest that soil blocks between desiccation cracks remain saturated even after fracture formation.

3.4. Perimetric Desiccation Crack

Tomograms show the formation of a fracture around the perimeter at relatively low suction ψ< 100 kPa, possibly due to a combination of a higher contact angle against the aluminum wall and larger pore sizes between the clay particles and the cell wall (Fig. 3). Eventually, the specimen separates completely from the lateral cell walls, i.e., lateral shrinkage and radial strain ε_r. We obtain the vertical strain ε_z from LVDT measurements and the volumetric strain ε_v from tomograms. Then, the radial strain is $\varepsilon_r = (\varepsilon_v - \varepsilon_z)/2$. Fig. 6 shows the radial strain plotted against the vertical strain. The initial 1D consolidation (Phase I) shows the increase in vertical strain ε_z proportional to the vertical stress σ'_z while the radial strain is ε_r= 0. The formation of the

perimetric fracture along the cell wall corresponds to the radial contraction with almost no vertical strain (Phase II). During the second drying stage ψ> 100 kPa, the sediment separated from the cell wall experiences no side friction, and the vertical strain increases proportionally to the radial strain (Phase III). The biasing vertical load affects the strain ratio $\varepsilon_z/\varepsilon_r$: $\varepsilon_z/\varepsilon_r$= 1.02 for σ'_{z0}= 10 kPa, $\varepsilon_z/\varepsilon_r$= 1.11 for σ'_{z0}= 20 kPa, and $\varepsilon_z/\varepsilon_r$= 1.30 for σ'_{z0}= 50 kPa.

3.5. Gas Bubbles

We label individual air bubbles and track their evolution during loading and desiccation (Fig. 7a – tracked bubbles range from 1 mm^3 to 10 mm^3, i.e., the number of voxels per bubble > 1200). Fig. 7b shows the total volume of gas bubbles in the three specimens plotted versus water content. Air bubbles shrink during both loading and early stages of desiccation: the total volume of bubbles reduces by approximately 40% before the water content at the AEV (Fig. 7b). There is a small volume increase after the AEV, however, changes are within the measurement precision.

3.6. Internal Desiccation Cracks

Internal desiccation cracks form in the three specimens at a suction near the air entry value AEV (see sequences in Fig. 4 and detailed cross sections in Fig. 8). Typical internal desiccation cracks are 5 mm to 15 mm long with an aperture of ~0.3 mm (resolution limited). The spacing between these cracks is larger than their length (Fig. 8a). Cracks have a planar or curved surface and irregular 3D morphology (Fig. 8b). All cracks are associated with one or more air bubbles that served as nucleation sites (Fig. 8c). The nucleation of 2 or 3 cracks at 120º are common (Fig. 8d). We also observe multiple cases of dual-parallel cracks that cannot be justified as imaging artifacts. Large vertical cracks (length up to 30 mm) develop from the interface with porous stone in spite

153 of the high frictional confinement. While suction controls the effective stress, the applied vertical
154 stress biases crack growth and favors vertical alignment as observed in tomograms.

155 **4. Analyses of Gas Bubbles and Internal Cracks**

156 The volume of a cavity contracts when the host medium experiences isotropic confining
157 stress (Fig. 7b inset – Timoshenko & Goodier, 1951); this mechanical analogy explains the
158 observed bubble contraction during early desiccation and shrinkage (Fig. 7b). Contraction leads to
159 the increase in gas pressure u_b inside the bubble (if the gas does not dissolve), which becomes
160 higher than the air pressure u_{air} outside the specimen. Yet, the water pressure u_w is quasi-constant
161 throughout the specimen during slow drying. Then, the Kirsch solution for a circular hole in a 2D
162 infinite plate predicts that the tangential stress on the bubble wall would become tensile when (u_b-
163 u_w)≥2(u_{air}-u_w) (Jaeger et al., 2009).

164 Increased gas pressure eventually leads to gas invasion at a large pore along the bubble
165 surface; this is the initiation of an internal crack. The sequence of particle-scale events resembles
166 the formation of desiccation cracks at the free surface (Fig. 9 – Shin & Santamarina, 2011a): (a)
167 capillary forces at the air-water interface on the bubble surface convert into skeletal interparticle
168 forces within the sediment, (b) the soil contracts and the granular skeleton stiffens, (c) suction
169 continuous increasing and the air-water interface invades the soil at the largest pores around the
170 bubble surface, (d) membrane invasion alters particle forces and causes grain displacement,
171 enlarges local pores and facilitates further membrane invasion leading to crack growth.

172 Note that air entry does not alter the fabric in stiff, coarse-grained sediments, however, air
173 entry is grain-displacive in soft, fine-grained sediments. Force equilibrium between grain-scale
174 capillary forces and effective stress-dependent skeletal forces defines the transition from grain-

displacement to pore-invasion, as captured in the dimensionless ratio $\Pi_{inv}=10\cdot T_s/(\sigma'\cdot d_{grain})$ where T_s is the surface tension, d_{grain} is the particle size, σ' is the effective stress (Shin & Santamarina, 2011b).

We recognize that the complexity of natural processes exceeds the plain macro- and particle-scale analyses proposed above. In fact, we do not address differences in volume contraction between bubbles and the sediment, and also disregard time dependent water pressure diffusion throughout the medium. Internal desiccation cracks are open-mode discontinuities; their initiation and growth reflect hydro-mechanical coupling and depend on many factors such as mechanical boundary conditions and principal stress directions, bubble size and shape, and bubble-bubble interactions. However, these analyses are an attempt to elucidate the essential processes behind internal desiccation crack formation.

5. Conclusions

This study explored the possibility of internal desiccation crack formation in soils. We tested water-saturated kaolinite specimens (with a few entrapped gas bubbles for potential nucleation sites), and used X-ray tomography to observe the evolution of consolidation and desiccation in self-reacting oedometer cells that reproduce various burial depths.

Air enters along the cell wall first due to higher contact angle and larger pore sizes. The perimetric crack detaches the specimen from cell walls; thereafter, the vertical strain increases proportional to the horizontal strain as suction increases.

Entrained gas bubbles shrink together with the specimen during early stages of desiccation, as theoretically predicted for a cavity inside a host medium subjected to isotropic confinement. The gas pressure inside bubbles increases during contraction. Eventually, the gas-water interface penetrates the soil at the largest pores around the bubble surface. Capillary forces at the air-water (soil) interface convert into skeletal interparticle forces within the sediment. Then, invasion of the interfacial membrane pushes particles away from the crack tip, enlarges local pores and facilitates further growth of the internal desiccation crack.

While air entry is grain-displacive in soft fine-grained sediments, it becomes pore-invasive in stiff coarse-grained sediments. Thus, internal desiccation cracks are not expected in silts or sands.

Acknowledgments

This research was funded by the KAUST endowment. G. E. Abelskamp edited the manuscript.

References

Campbell, G. S., Smith, D. M., & Teare, B. L. (2007). Application of a dew point method to obtain the soil water characteristic. *Experimental unsaturated soil mechanics*. Springer, Berlin, Heidelberg, 71-77.

Cordero, J. A., Useche, G., Prat, P. C., Ledesma, A., & Santamarina, J. C. (2017). Soil desiccation cracks as a suction–contraction process. *Géotechnique Letters* **7**, No. 4, 279-285.

Corte, A., & Higashi, A. (1964). Experimental research on desiccation cracks in soil (No. RR-66). *U.S. Army Cold Regions Research and Engineering Laboratory*, NH United States.

Dyer, M., Utili, S., & Zielinski, M. (2009, June). Field survey of desiccation fissuring of flood embankments. *Proceedings of the Institution of Civil Engineers-Water Management* **162**, No. 3, 221-232. Thomas Telford Ltd.

Espinoza, D. N., & Santamarina, J. C. (2012). Clay interaction with liquid and supercritical CO2: The relevance of electrical and capillary forces. *International Journal of Greenhouse Gas Control* **10**, 351-362.

Harris, R. C. (2004). Giant desiccation cracks in Arizona. Open-file report 04-01. *Tucson: Arizona Geological Survey*.

Jaeger, J. C., Cook, N. G., & Zimmerman, R. (2009). Fundamentals of rock mechanics 4th ed. *Blackwell Publishing Ltd, MA, USA*.

Jang, J., & Santamarina, J.C. (2015). Fines classification based on sensitivity to pore-fluid chemistry. *Journal of Geotechnical and Geoenvironmental Engineering* **142**, No. 4, 06015018.

Khalili, N., Habte, M.A., & Zargarbashi, S. (2008). A fully coupled flow deformation model for cyclic analysis of unsaturated soils including hydraulic and mechanical hystereses. *Computers and Geotechnics* **35**, No. 6, 872-889.

Ledesma, A., Lakshmikantha, M. R., & Prat, P. C. (2018). Boundary Effects in the Desiccation of Soil Layers with Controlled Environmental Conditions. *Geotechnical Testing Journal*, **41**, No. 4, 675-697.

Liao, P. S., Chen, T. S., & Chung, P. C. (2001). A fast algorithm for multilevel thresholding. *Journal of Information Science and Engineering* **17**, No. 5, 713-727.

Ortiz, L., Volckaert, G., & Mallants, D. (2002). Gas generation and migration in Boom Clay, a potential host rock formation for nuclear waste storage. *Engineering geology* **64**, No. 2-3, 287-296.

Plummer, P. S., & Gostin, V. A. (1981). Shrinkage cracks: desiccation or synaeresis? *Journal of Sedimentary Research*, **51**, No. 4, 1147-1156.

Pratt, B. R. (1998). Syneresis cracks: subaqueous shrinkage in argillaceous sediments caused by earthquake-induced dewatering. *Sedimentary Geology*, **117**, No. 1, 1-10.

Rebata-Landa, V., & Santamarina, J. C. (2012). Mechanical effects of biogenic nitrogen gas bubbles in soils. *Journal of Geotechnical and Geoenvironmental Engineering* **138**, No. 2, 128-137.

Scherer, G. W. (1990). Theory of drying. *Journal of the American Ceramic Society* **73**, No. 1, 3-14.

Shin, H., & Santamarina, J. C. (2011a). Desiccation cracks in saturated fine-grained soils: particle-level phenomena and effective-stress analysis. *Géotechnique* **61**, No. 11, 961-972.

Shin, H., & Santamarina, J. C. (2011b). Open-mode discontinuities in soils. *Géotechnique Letters* **1**, No. 4, 95-99.

Sherard, J. L. (1986). Hydraulic fracturing in embankment dams. *Journal of Geotechnical Engineering* **112**, No. 10, 905-927.

Timoshenko, S., & Goodier, J. N. (1951). *Theory of elasticity*. New York: McGraw-Hill.

256 Vanapalli, S. K., Fredlund, D. G., & Pufahl, D. E. (1996). The relationship between the soil-water
257 characteristic curve and the unsaturated shear strength of a compacted glacial till.
258 *Geotechnical Testing Journal* **19**, No. 3, 259-268.

259 Wheeler, S. J., Sharma, R. S., & Buisson, M. S. R. (2003). Coupling of hydraulic hysteresis and
260 stress–strain behaviour in unsaturated soils. *Géotechnique* **53**, No. 1, 41-54.

261 Yesiller, N., Miller, C. J., Inci, G., & Yaldo, K. (2000). Desiccation and cracking behavior of three
262 compacted landfill liner soils. *Engineering Geology* **57**, No. 1-2, 105-121.

263

Figures

Fig. 1. Soil water retention curve for the kaolinite used in this study. Suction values measured using a chilled-mirror hydrometer.

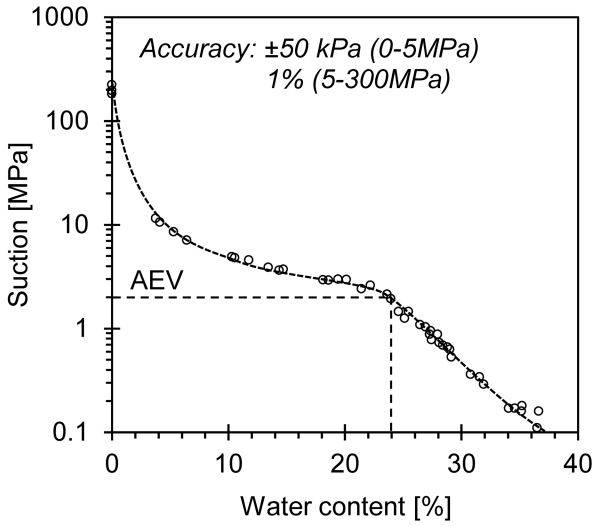

270 Fig. 2. Self-reactive, X-ray transparent oedometer cell.

271

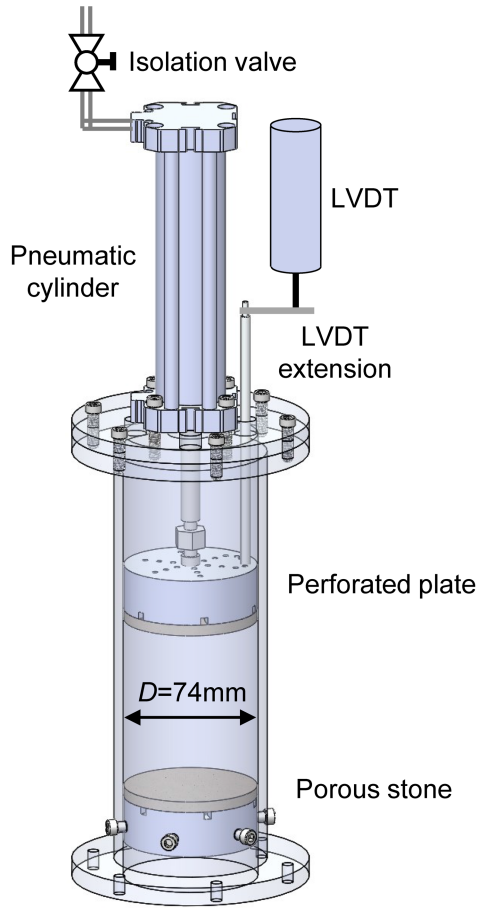

272

273

Fig. 3. Water content and vertical strain evolution during consolidation and drying. The open circles shown on the vertical strain curves identify scanning events.

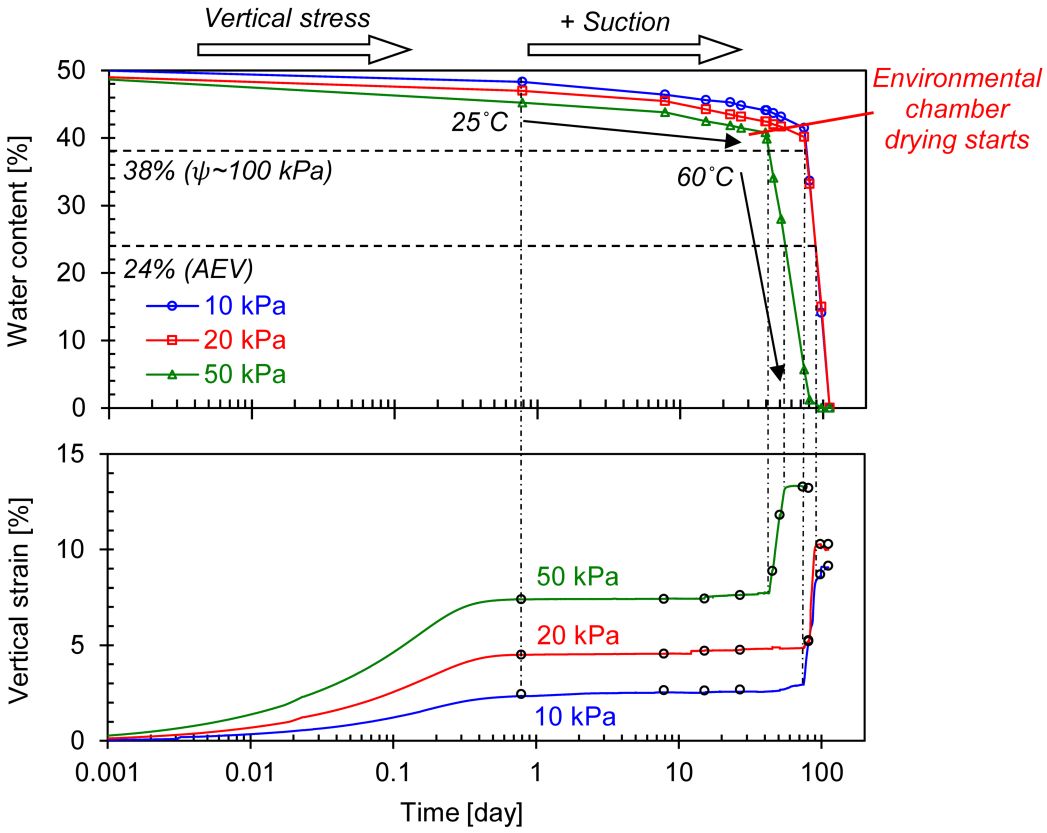

279 Fig. 4. Two slices of the 3D tomogram gathered at different depths. Evolution during drying.

280 Specimen subjected to σ'_{z0}= 10 kPa. Arrows mark internal cracks and their origin at gas bubbles.

281 Note: light grey= aluminum cylinder; grey= kaolinite pastes; black= air voids.

282

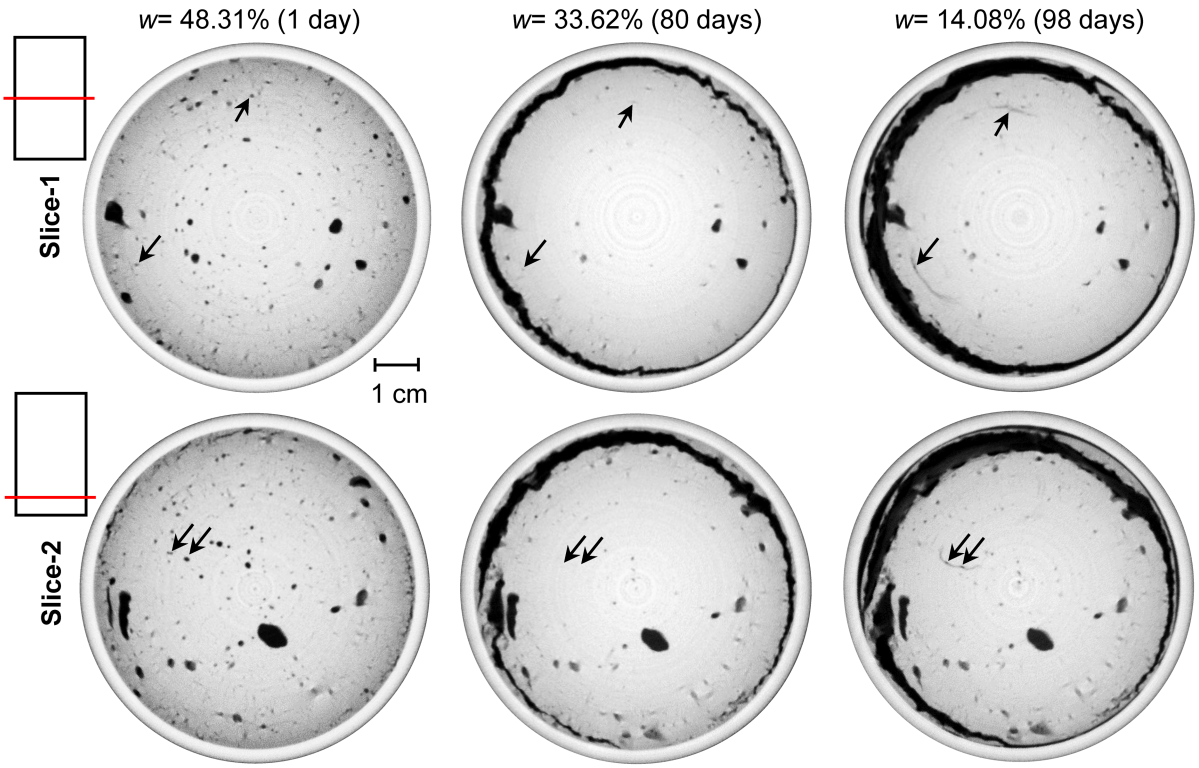

283

284

285 Fig. 5. Volume contraction during loading and desiccation. Void ratio versus Bishop's effective

286 stress $\sigma'_B = (\sigma - u_a) + \chi(u_a - u_w)$ computed assuming $\chi = 1.0$.

287

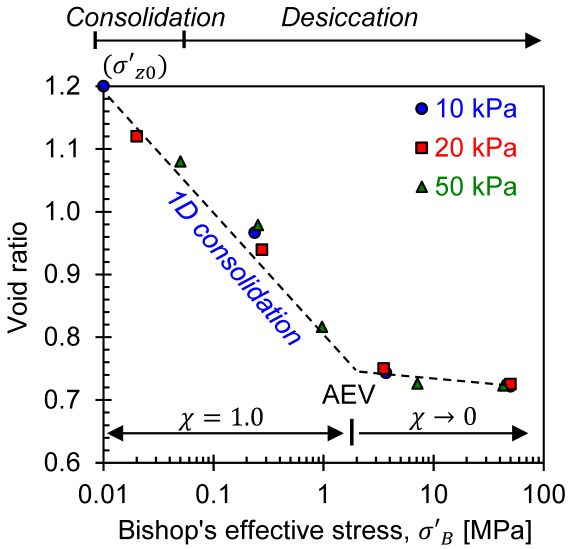

288

289

290 Fig. 6. Vertical and radial strains. Evolution during (I) stress-controlled consolidation, (II)
291 formation of perimetric fracture, (III) further contraction during desiccation.

292

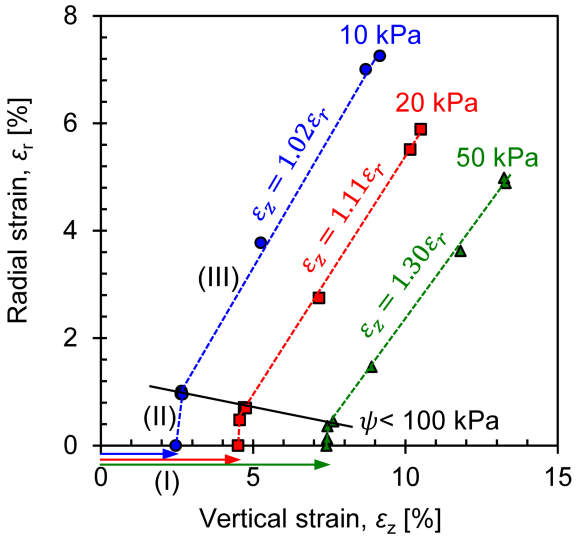

293

294

295 Fig. 7. Evolution of gas bubbles. (a) Identified and labelled gas bubbles ($V \geq 1$ mm^3) for the
296 specimen subjected to $\sigma'_{z0} = 20$ kPa; tomographic image gathered at $w = 47\%$. (b) Evolution of the
297 total volume of gas bubbles during drying for the three specimens. (b-inset) Radial stress σ_a and
298 hoop stress σ_h in a spherical thick-wall volume under the same external and internal pressure p
299 (Timoshenko & Goodier, 1951).

300

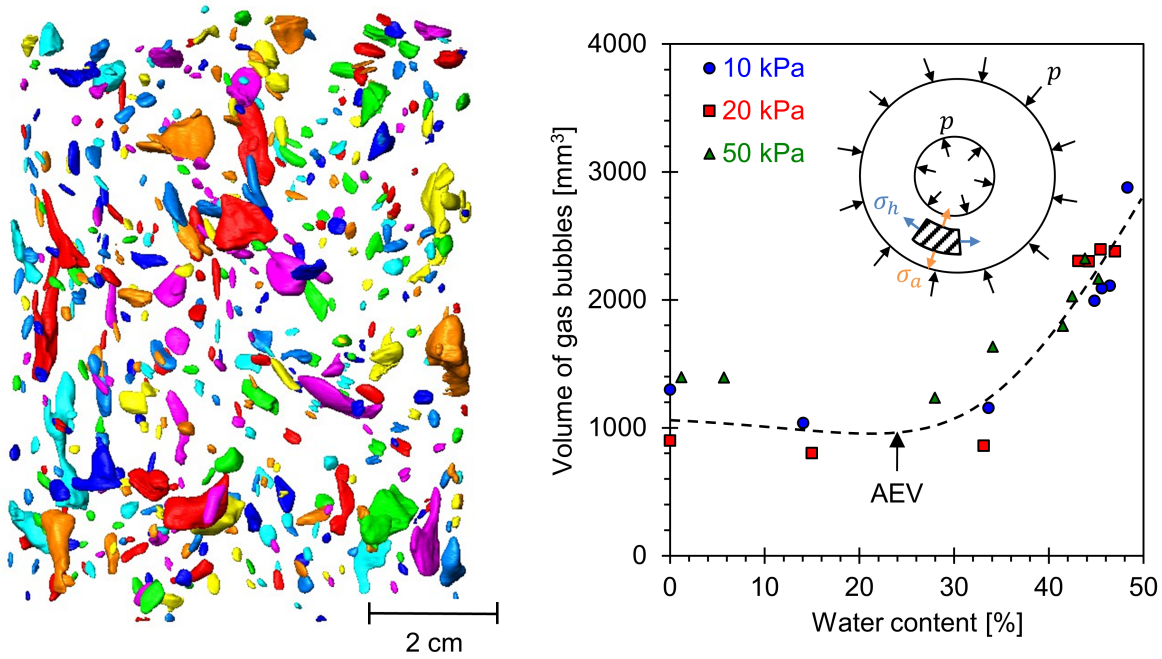

301

302

303 Fig. 8. Internal desiccation cracks. Images obtained at an estimated suction of 3.5 MPa (for
304 reference, the suction value at air entry is ψ_{AE}= 2 MPa). (a) Internal cracks. (b) 3D morphology.
305 (c) Gas bubbles as nucleation sites. (d) Nucleation at 120° and dual-parallel cracks.

306

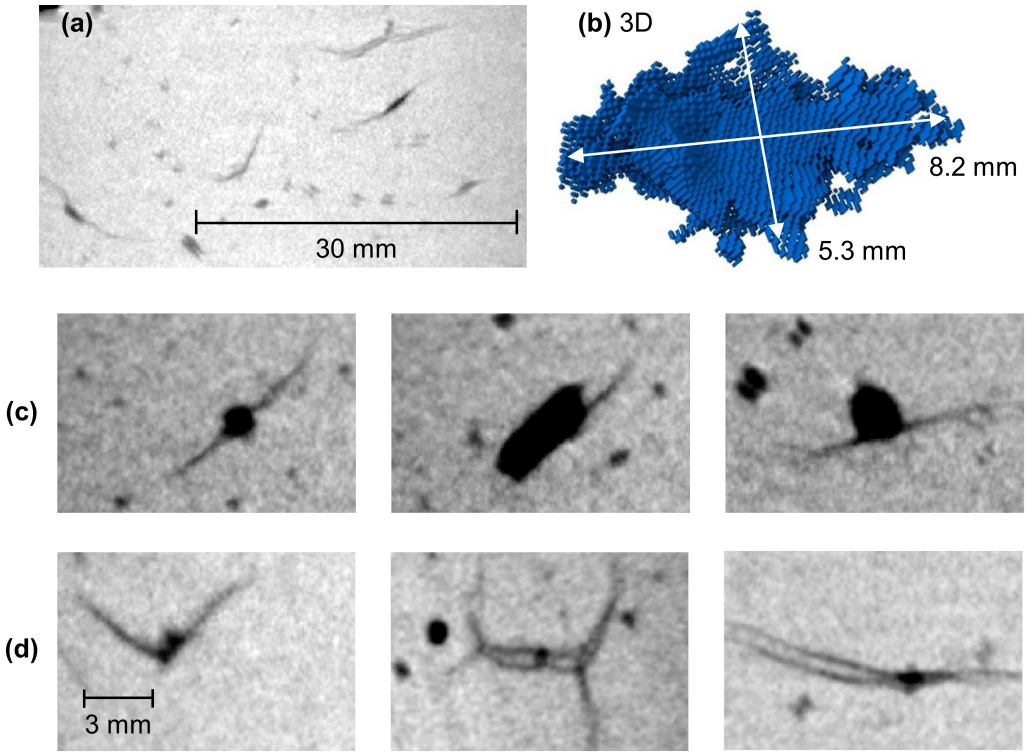

307

308

309

Fig. 9. Macro-scale and particle-scale analysis of internal desiccation crack formation. (a-b) Suction-controlled shrinkage. (b-d) Crack nucleation and growth.